Dynamic Origin of the Interannual Variability of West China Autumn Rainfall

ZHIWEI ZHU,[a] RUI LU,[a] HUIPING YAN,[a] WENKAI LI,[a] TIM LI,[a,b] AND JINHAI HE[a]

[a] *Key Laboratory of Meteorological Disaster, Ministry of Education/Joint International Research Laboratory of Climate and Environment Change/Collaborative Innovation Center on Forecast and Evaluation of Meteorological Disasters, Nanjing University of Information Science and Technology, Nanjing, China;* [b] *International Pacific Research Center and Department of Atmospheric Sciences, University of Hawai'i at Mānoa, Honolulu, Hawaii*

(Manuscript received 14 February 2020, in final form 15 June 2020)

ABSTRACT: The dynamic origin of the interannual variability of West China autumn rainfall (WCAR), a special weather/climate phenomenon over western-central China in September and October, was investigated via observational diagnosis and numerical simulations. Here we found that the interannual variability of WCAR is closely related to the local horizontal trough, which is passively induced by two lower-level anticyclonic (high pressure) anomalies over East Asia. The anticyclonic anomaly over the south is a Gill-type response to the central and eastern Pacific diabatic cooling, while that over the north is part of the mid- to high-latitude barotropic Rossby wave train, which could be induced by either the thermal forcing of the central and eastern Pacific Ocean sea surface temperature (SST) cooling or that of the subtropical northern Atlantic Ocean SST warming. The quasi-barotropic high pressure anomaly over East Asia acts as an ''invisible mountain'' that steers the low-level anomalous southwesterly into a southeasterly and hinders the water vapor going farther to the north, leading to enhanced WCAR. However, the real mountain ranges in the region (the Qinglin and Ba Mountains) have no essential impact on the formation and interannual variability of WCAR.

KEYWORDS: Atmosphere-ocean interaction; Orographic effects; Stationary waves; Teleconnections; Interannual variability

1. Introduction

West China autumn rainfall (WCAR) is a special weather/climate phenomenon occurring over western-central China from late August to early November (Liang 1989; Bai and Dong 2004). It is the last stage of the rainy season over China during the seasonal march of the East Asian summer monsoon, and it indicates the commencement of the East Asian winter monsoon (Gao and Guo 1958). WCAR has profound and complex impacts on agricultural production. For example, a deficient WCAR will often result in severe drought during the following spring owing to the low water level in numerous reservoirs in the region, while an excessive WCAR and corresponding reduced sunlight can damage the roots of crops and inhibit photosynthesis, leading to low crop production. In addition, because WCAR falls over mountainous terrain, it inevitably causes landslides and debris flows, which pose great threats to human life, economy, and ecosystems.

Previous studies have elucidated the statistical characteristics of WCAR. The climatology of its location and timing has been investigated (Gao and Guo 1958; Liang 1989; Bai and Dong 2004). It is suggested that WCAR has two leading modes, one with homogeneous changes in the region and the other with out-of-phase variations between the east and west parts of the region (Luo et al. 2013). WCAR features prominent interannual and interdecadal changes, with the associated number of rainy days and the rainfall amount showing both a significant deceasing trend before 2000 (Ma et al. 2013; Sun et al. 2013; Li et al. 2015; Zhang et al. 2018) and an obvious strengthening in the twenty-first century (Jiang et al. 2014; Wang et al. 2018; Wang and Zhou 2019).

The typical atmospheric circulations associated with autumn rainfall over China include a strengthened western Pacific subtropical high (Niu and Li 2008; Li et al. 2017), the establishment of the westerly jet stream over East Asia (Luo et al. 2013), and strong westerlies over the southern rim of the Tibetan Plateau (Chen et al. 2001). The underlying physical mechanisms by which these associated circulation systems form have also been revealed. For instance, they have been linked with the sea surface temperature (SST) anomalies (SSTA) in the tropical Pacific, such as El Niño–Southern Oscillation and the Indian Ocean Dipole pattern (Liu and Yuan 2006; Xiao et al. 2015; Xu et al. 2016; Hu et al. 2018), the east–west thermal contrast over the tropical Pacific (Gu et al. 2015; Zhao et al. 2000; Ting et al. 2018; Wang et al. 2015), and the thermal conditions of the Tibetan Plateau (Ji and Xu 1990; Chen et al. 2001). However, an in-depth understanding of the mechanisms of WCAR variabilities remain notably absent.

Consensus is yet to be reached regarding the definition of WCAR in terms of both its timing and domain. Figure 1 plots the climatology of the distribution of daily rainfall rate over China during the autumn season. It can be seen that, during September, except for the southeast coastal region where there is considerable influence from the prevailing western North Pacific tropical cyclones, most significant rainfall is mainly concentrated over the regions of southern Gansu, southern Shaanxi, southwestern Henan, western Hubei, Sichuan, and Chongqing. In October, the coastal rainfall largely disappears,

Supplemental information related to this paper is available at the Journals Online website: https://doi.org/10.1175/JCLI-D-20-0097.s1.

Corresponding author: Dr. Zhiwei Zhu, zwz@nuist.edu.cn

DOI: 10.1175/JCLI-D-20-0097.1

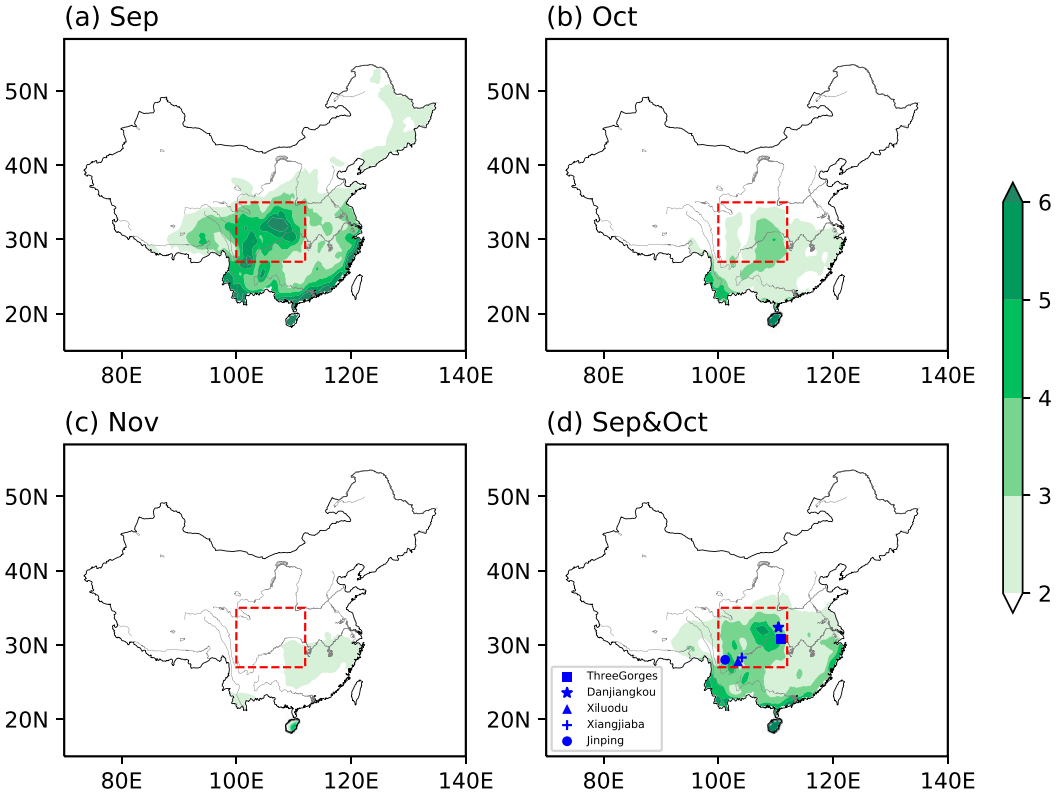

FIG. 1. Climatological mean of the precipitation (shading; mm day^{-1}) over China in (a) September, (b) October, (c) November, and (d) the average of September and October. The red dashed box (100°–112°E, 27°–35°N) denotes the domain of WCAR. The locations of five world-renowned dams (Three Gorges, Danjiangkou, Xiluodu, Xiangjiaba, and Jinping) are shown with different symbols in blue in (d).

but the maximum inland rainfall over western-central China remains, albeit with a largely weakened intensity. In November, no significant rainfall can be observed over most of China. Based on this climatological feature of the rainfall distribution, we defined WCAR as the mean of the September and October rainfall over the domain (100°–112°E, 27°–35°N) (red dashed box in Fig. 1), where the maximum autumn daily rainfall rate is found. Note that, different to the rain belt during spring and summer, which is mainly confined to southern China and the middle and lower reaches of the Yangtze River basin (Zhu et al. 2012; Sun and Wang 2015, Sun et al. 2019), respectively, the autumn rain belt is located over the upper and middle reaches of the Yangtze River basin. Hundreds of dams, including five of the world's largest dams (Three Gorges, Danjiangkou, Xiluodu, Xiangjiaba, and Jinping), have been built in the WCAR region (blue marks in Fig. 1d). Therefore, the variability of WCAR will directly determine policies related to water conservancy and hydroelectric power during the following seasons.

Thus far, the characteristics of boreal spring and summer rainfall over East Asia have been extensively studied (Zhu et al. 2014; Chen et al. 2019; Lu et al. 2020), and the framework of the air–sea coupling between the western Pacific subtropical high and the tropical Pacific/Indian Ocean SSTA on the interannual time scale has been clearly unraveled (Wang et al. 2000; Xie et al. 2009; Wu et al. 2009). However, the air–sea interaction affecting the interannual rainfall variability during the autumn season, particularly for WCAR, remains elusive. Besides, whether the mountainous terrain plays a vital role in the formation of WCAR has for a long time remained an unanswered question (Lu 1944).

Aside from the general lack of knowledge with respect to WCAR, AMIP-type simulations (driven by the historical SST) of the interannual variability of WCAR using state-of-the-art atmospheric general circulation models have been quite unsuccessful (Fig. 2a). None of them can capture the variability of WCAR either in terms of its fluctuation or intensity (Fig. 2b). Therefore, to advance our understanding of the dynamic origins of WCAR and improve its seasonal prediction, the aim of the present study was to address the following three questions: What are the key circulation systems controlling the variabilities of WCAR? What is the fundamental physical process affecting the key circulation systems? Does the mountainous terrain play an important role in the formation of WCAR?

The rest of the paper is organized as follows: Section 2 introduces the datasets, methods, and the model used in this study. In section 3, we investigate the circulation and SST anomaly fields associated with the interannual variability of WCAR. The origins of variabilities are detected and verified via both observational diagnosis and numerical simulations. In section 4, the effect of the mountainous terrain on WCAR is

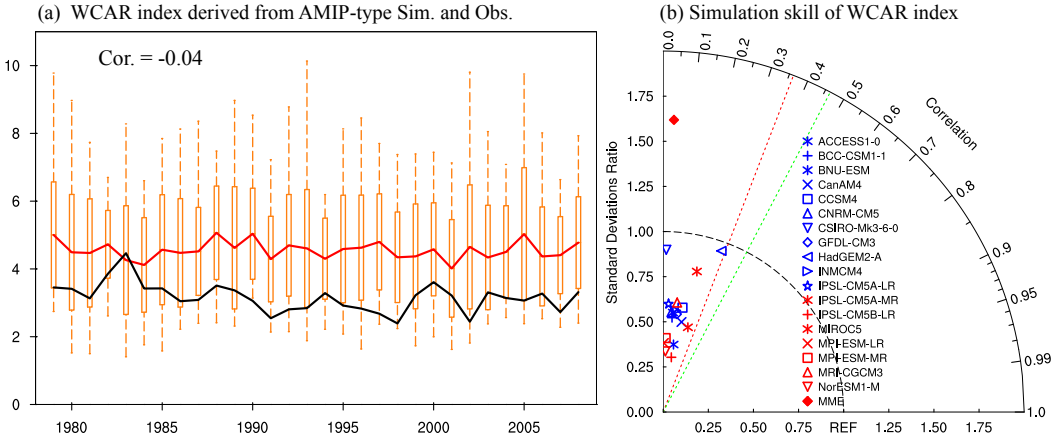

FIG. 2. (a) Time series of WCAR index derived from AMIP5 models (red line denotes the MME result; boxes denote 1 standard deviation of the models; dashed lines denote the spread of the models) and observation (black line) during 1979–2008. (b) Taylor diagram showing the simulation performance of the year-to-year variation of WCAR derived from each model in terms of standard deviation ratio (using standard deviation in observation divided by that of model outputs) and temporal correlation (red and green dashed lines denote the 95% and 99% confidence levels, respectively).

explored based on the Weather Research and Forecasting (WRF) Model. Concluding remarks are given in section 5.

2. Data, methods, and models

The datasets employed in this study were 1) monthly gauge precipitation data over China gridded to a horizontal resolution of 0.25° × 0.25° (Wu and Gao 2013); 2) monthly atmospheric field datasets with a horizontal resolution of 2.5° × 2.5° from the National Centers for Environmental Prediction–National Center for Atmospheric Research Reanalysis I (Kalnay et al. 1996); 3) monthly mean SST data gridded to a 2.0° × 2.0° horizontal resolution from the improved Extended Reconstructed SST dataset, version 5 (Huang et al. 2017); and 4) global monthly precipitation data with a 2.5° × 2.5° horizontal resolution provided by the National Oceanic and Atmospheric Administration Precipitation Reconstruction (Chen et al. 2002). The time span of all datasets was from 1961 to 2017.

The WCAR index is defined as the autumn mean (September and October) precipitation over the domain of 100°–112°E, 27°–35°N based on the climatological precipitation pattern as shown in Fig. 1. The coherent of the interannual variability in each grid of the domain is checked by the correlation coefficient map between WCAR index and simultaneous precipitation in each grid over China (see Fig. S1 in the online supplemental material). Almost all the grids in the domain show the coherent interannual variability with the WCAR index. Moreover, we also do the sensitivity experiments by using the slightly changed domains (e.g., 102°–114°E, 27°–35°N; 98°–108°E, 27°–35°N; 100°–112°E, 26°–34°N; 100°–112°E, 28°–36°N). The differences among the defined WCAR indices can be neglected. Therefore, our definition on the domain of WCAR is objective and reasonable. The interdecadal variability of WCAR was obtained by a 9-yr running mean of the raw WCAR variation, while the interannual variability of WCAR was extracted by removing the interdecadal variability from the raw WCAR variation. Linear regression analysis was employed to explore the relationship between dynamical and thermal–dynamical fields and WCAR, and the Student's t test was applied to assess the statistical significance.

To understand the origin and the large-scale atmospheric circulation associated with the interannual variability of WCAR, the phase-independent wave activity flux (WAF) was calculated based on the following formula by Takaya and Nakamura (2001):

$$\mathbf{W} = \frac{1}{2|\overline{\mathbf{U}}|}\begin{bmatrix} \overline{u}(\psi_x'^2 - \psi'\psi_{xx}) + \overline{v}(\psi_x'\psi_y' - \psi'\psi_{xy}) \\ \overline{u}(\psi_x'\psi_y' - \psi'\psi_{xy}) + \overline{v}(\psi_y'^2 - \psi'\psi_{yy}) \end{bmatrix},$$

where an overbar and a prime represent the climatological mean and anomaly, respectively; ψ and $\mathbf{U} = (u, v)$ represent the streamfunction and the horizontal wind, respectively; and $\mathbf{W}$ denotes the two-dimensional Rossby WAF.

To unravel the physical process of the variability of WCAR, an atmospheric general circulation model—ECHAM4.6 (Roeckner et al. 1996) was employed in this study. ECHAM4.6 is developed by the Max Planck Institute for Meteorology, which has a horizontal resolution of around 2.88 × 2.88 (T42) and 19 vertical levels extending from the surface to 10 hPa. The control and sensitivity experiments in this study were both integrated for 20 years, with slightly different initial conditions for each year, and the last 15 years composite differences of model outputs were used to represent the climatic response to the prescribed forcing. Besides, the NCAR Advanced Research version of WRF (WRF-ARW, version 3.5) was also employed to examine the impacts of the mountainous terrain on the formation of WCAR. The model domain was centered at (32°N, 110°E) and covered an area of 150 (west–east) ×120 (south–north) grid cells with 25-km horizontal resolution. There were 38 levels in the vertical direction. The Kain–Fritsch scheme for convective parameterization (Kain 2004), RRTMG for shortwave and longwave radiation (Iacono et al. 2008), Morrison 2 momentum scheme for cloud microphysics (Morrison

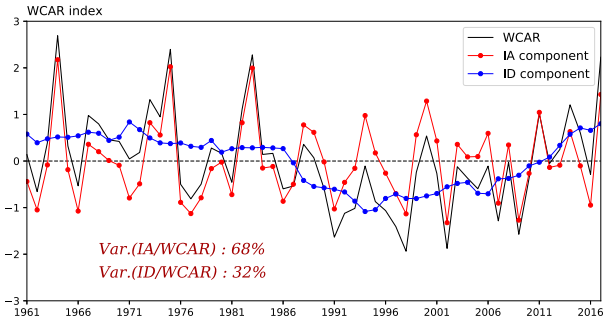

FIG. 3. Time series of normalized year-to-year WCAR index (black line) and its interannual (red line) and interdecadal (blue line) components.

et al. 2009), YSU PBL scheme (Hong et al. 2006), and Noah land surface model were employed to run the model. WRF-ARW is driven by atmospheric and surface forcing data extracted from the NCEP Final (FNL) Operational Model Global Tropospheric Analyses.

3. Origin of the interannual WCAR

Figure 3 shows the time series of the year-to-year WCAR variability. The interannual component accounts for 68% of the total variance of year-to-year WCAR variability. In this study, we only focused on the interannual variability of WCAR.

To investigate the associated circulation anomalies with respect to the interannual WCAR, Fig. 4 plots the wind and geopotential height fields at 850 and 200 hPa regressed onto interannual WCAR index. At 850 hPa (Fig. 4a), East Asia is characterized by the two pronounced anticyclonic (high pressure) anomalies centered over the western North Pacific and Northeast China, respectively. To the west of the two anticyclonic anomalies is a large-scale low pressure anomaly. Note that a horizontal trough appears over the east of the Tibetan Plateau and it is oriented in between the two anticyclonic anomalies. To the south of the trough, southwesterlies could transport water vapor from the tropical oceans (see Fig. S2 in the online supplemental material). To the north of the trough, southeasterlies appear, leading to cyclonic wind shear in the region and enhanced WCAR. Over the upper level of 200 hPa, a robust positive geopotential height (anticyclonic) anomaly controls almost the whole of China with its center located to the northeast of the WCAR domain (Fig. 4b). The largest horizontal divergence appears at 200–150 hPa, which corresponds to the maximum positive geopotential height anomaly (see Fig. S3 in the online supplemental material), whereas the largest ascending motion anomaly appears in 250–500 hPa, suggesting the high pressure anomaly over the upper

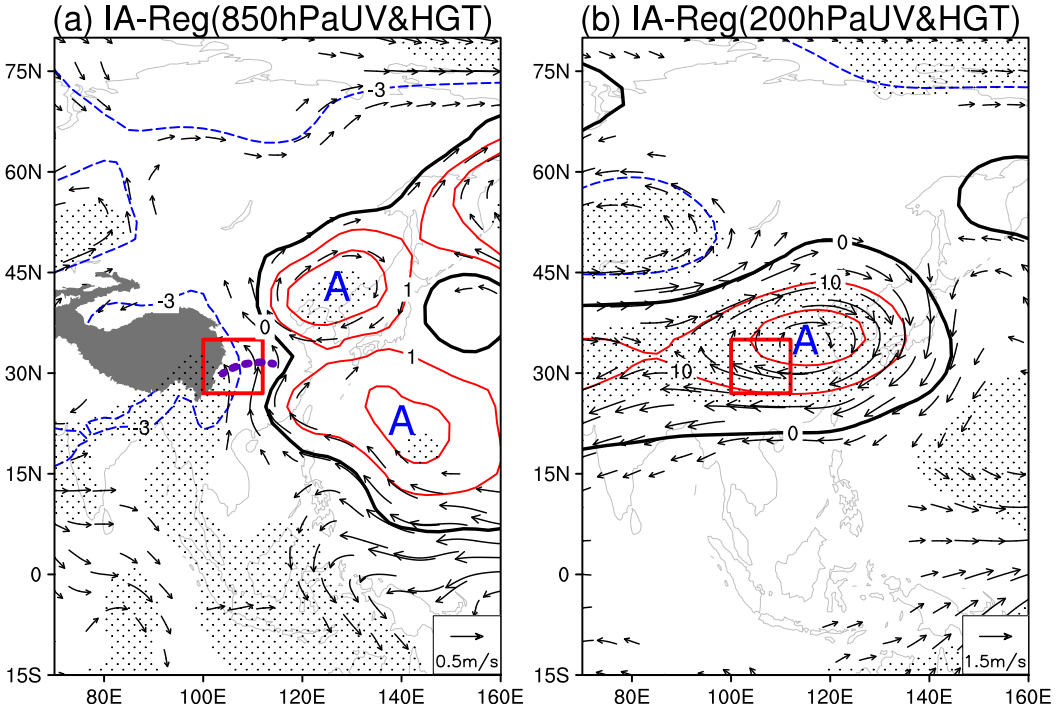

FIG. 4. Wind (vectors; m s^{-1}, only vectors that pass the 95% significant level are shown) and geopotential height (contours; gpm) fields at (a) 850 and (b) 200 hPa regressed onto the interannual variability of WCAR. The purple marks in (a) indicate the horizontal trough, and shading denotes the Tibetan Plateau. Thick black contours denote zero regression coefficients of geopotential height. The letter A denotes the center of the anticyclonic anomaly, and the red-outlined box denotes the WCAR domain. Stippling marks regression coefficients of the geopotential height that pass the 95% significance level.

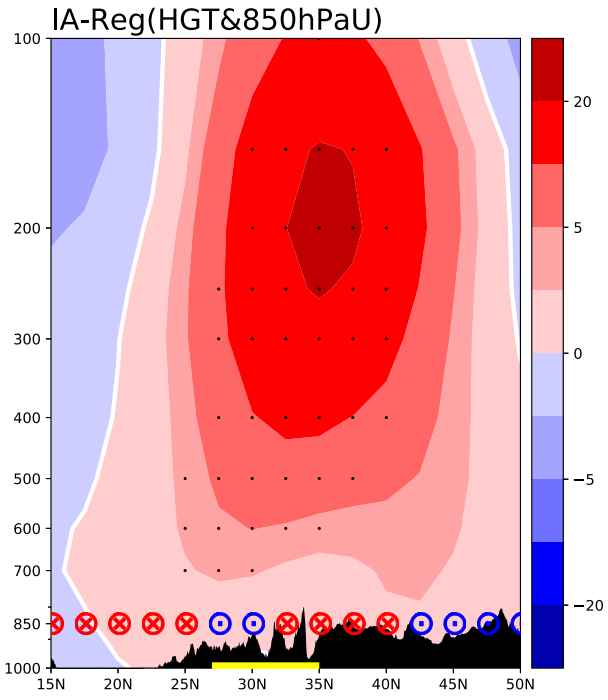

FIG. 5. Vertical–latitude profile of geopotential height (contours; gpm), and zonal wind direction at 850 hPa (red crosses and blue dots denote anomalous easterly and westerly, respectively) regressed onto the interannual variability of WCAR averaged over 115°–130°E. The black shading indicates the topography, and black dots mark the regression coefficients that pass the 95% significance level. The yellow bar denotes the WCAR domain.

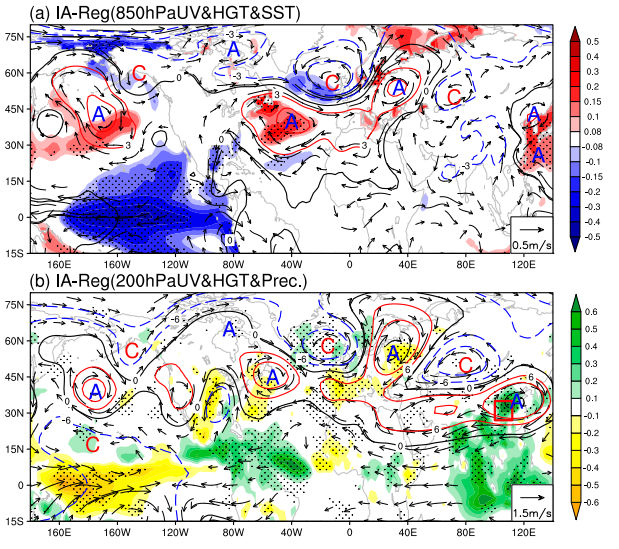

FIG. 6. (a) Wind (vectors; m s^{-1}, only vectors that pass the 95% significant level are shown) and geopotential height (contours; gpm) at 850 hPa and SST (shading; °C) fields regressed onto the interannual variability of WCAR. (b) Wind and geopotential height at 200 hPa and precipitation (shading; mm day^{-1}) fields regressed onto the interannual variability of WCAR. Black contours denote zero regression coefficients of geopotential height. The letters A and C denote the centers of the anticyclonic and cyclonic anomalies, respectively, and the red-outlined box denotes the WCAR domain. Stippling marks the regression coefficients of SST/precipitation that pass the 95% significance level.

level could also enhance uplift flow and WCAR through the pumping effect.

Figure 5 plots the vertical–longitude cross section of the geopotential height. At the first glance, one may find a pronounced high pressure anomaly dominating over the entire troposphere in the region. However, after careful scrutiny, two independent anomalous high pressure (anticyclonic) centers can be observed at the lower level (850 hPa) corresponding to Fig. 4a, and they are significantly different in nature. The high pressure (anticyclonic) anomaly to the south of 32°N corresponds to a low pressure anomaly in the upper troposphere, presenting a baroclinic structure (Fig. 4b). On the contrary, the high pressure (anticyclonic) anomaly to the north as shown in Fig. 5 is more like a downward extension of the quasi-barotropic high pressure (anticyclonic) anomaly (Fig. 4b).

From the above analysis, we concluded that enhanced WCAR is closely related to the cyclonic wind shear or the horizontal trough in the lower troposphere. The horizontal trough is directly corresponding to the two anticyclonic (high pressure) anomalies centered over the western North Pacific and Northeast China, respectively. As shown in Fig. 5, the high pressure (anticyclonic) anomaly over Northeast China shows a robust quasi-barotropic structure, which acts as an ''invisible mountain.'' The invisible mountain (high pressure) anomaly hinders the southwesterly wind blowing further to the north, but steers the wind northwestwards, therefore leading to the horizontal trough and enhanced rainfall in the region. Thus, the question with regard to the origin of the interannual variability of WCAR can be refined to one of investigating from where the quasi-barotropic high pressure (anticyclonic) anomaly comes.

To study the formation of the quasi-barotropic high pressure anomaly, the large-scale dynamic and thermodynamic fields associated with the interannual of WCAR are plotted in Fig. 6. It can be seen that the quasi-barotropic high pressure anomaly over East Asia is part of the two mid- to high-latitude quasi-barotropic stationary Rossby wave trains (Fig. 6). One wave train is characterized by anticyclonic anomalies centered over the subtropical Atlantic, eastern Europe, and East Asia and cyclonic anomalies centered over the south of Iceland and central Asia. The other wave train has two anticyclonic anomalies centered over the North Pacific and northern Canada, and one cyclonic anomaly centered over/near to the Gulf of Alaska, and the rest of the wave train merges into the first Rossby wave train, with cyclonic anomalies centered over the south of Iceland and central Asia and anticyclonic anomalies centered over eastern Europe and East Asia.

A natural question arises as to what causes these two Rossby wave trains. Here, we speculate the SSTA forcing may play roles in their formation. As indicated by the significant correlation coefficients in Fig. 6a, the two Rossby wave trains can be traced back to SSTA over the tropical central and eastern Pacific Ocean (CEP) and subtropical Atlantic Ocean (SAT).

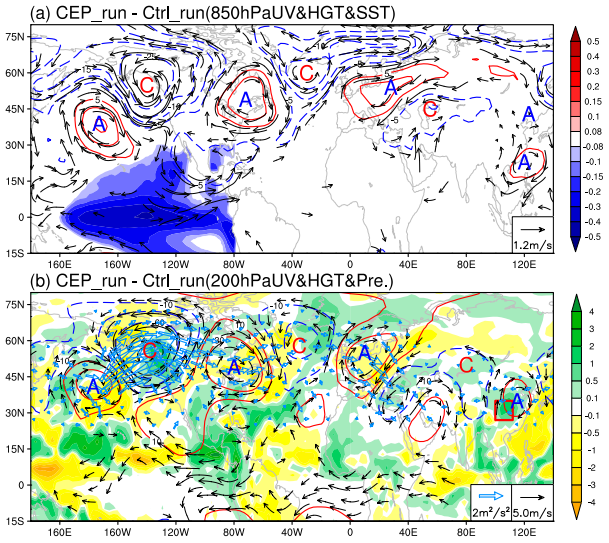

FIG. 7. (a) Wind (vectors; m s^{-1}) and geopotential height (contours; gpm) anomaly responses at 850 hPa to the observed central-eastern Pacific negative SSTA (shading; °C). (b) Wind (black vectors; m s^{-1}), wave activity flux (blue vectors; $m^2 s^{-2}$), geopotential height (contours; gpm) at 200 hPa, and precipitation (shading; mm day^{-1}) anomaly responses to the observed central-eastern Pacific negative SSTA. The letters A and C denote the centers of the anticyclonic and cyclonic anomalies, respectively. The red-outlined box denotes the WCAR domain.

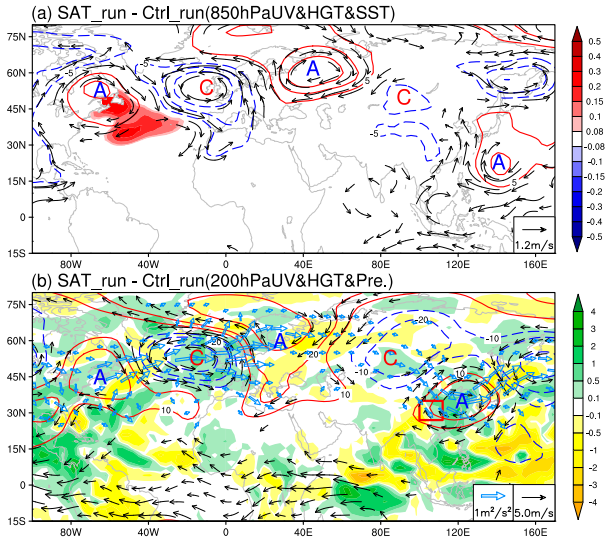

FIG. 8. As in Fig. 7, but for the observed subtropical Atlantic positive SSTA.

The CEP negative SSTA could induce suppressed rainfall (diabatic cooling) over the central equatorial Pacific (Fig. 6b). At 850 hPa (Fig. 6a), an anticyclonic anomaly is simulated to the northwest of the diabatic cooling in terms of the Gill–Matsuno response (Gill 1980; Matsuno 1966). To the northwestern flank of the anticyclonic anomaly, the southwesterly appears, favoring the moisture transportation of the WCAR. At 200 hPa (Fig. 6b), a cyclonic anomaly is observed to the north of the diabatic cooling as a Gill–Matsuno response. To the north of the cyclonic anomaly, an anticyclonic anomaly is perturbed, and then a downstream Rossby wave train is formed. Note that the atmospheric response becomes quasi-barotropic to the north of the cyclonic anomaly (30°N), suggesting the tropical diabatic cooling is the origin for the midlatitude Rossby wave train. Because of the waveguide of the subtropical westerly jet steam, the Rossby wave travels northeastward to northern North America, and then turns southeastward across the Eurasian continent before finally arriving in East Asia with its terminal of a quasi-barotropic high pressure (anticyclonic) anomaly, leading to enhanced WCAR.

The positive SSTA over the SAT does not induce a significant positive rainfall anomaly because the climatological mean state of SST over the SAT is quite low compared to that in the tropics (Fig. 6b). Therefore, despite being a significant positive anomaly, the absolute value of the SST over the SAT cannot stimulate local convective heating. However, the warming SSTA may induce a local barotropic high pressure (anticyclonic) anomaly via longwave radiative heating (see Fig. S4 in the online supplemental material). The barotropic high pressure (anticyclonic) anomaly perturbs the subtropical westerly jet stream and then stimulates the Rossby wave train from the North Atlantic to East Asia, leading to the quasi-barotropic high pressure (anticyclonic) anomaly that favors enhanced WCAR.

To support our hypothesis that both the CEP negative SSTA and the SAT positive SSTA could induce the quasi-barotropic Rossby wave train, and in turn the local upper-level anticyclonic anomaly and enhanced WCAR, two sensitivity experiments were conducted using the ECHAMv4.6 model. The first experiment (CEP_run) was conducted with the additional prescribed negative SSTA over the CEP, while the second one (SAT_run) was run by the additional positive SSTA over the SAT. The control experiment (Ctrl_run) was run using the historical climatological SST.

Figure 7 shows the circulation and rainfall response to the imposed CEP negative SSTA. It can be clearly seen that a Rossby wave train emanating from the northern tropical Pacific to East Asia can be nicely stimulated by the CEP SSTA cooling. At the lower level (850 hPa), the anticyclonic anomaly appears over the tropical western Pacific, being the Gill-type response to the diabatic cooling in the central Pacific, while another anticyclonic anomaly appears over northeast Asia, acting as the terminal of the induced mid- to high-latitude Rossby wave train. The two anticyclonic anomalies result in the cyclonic wind shear in the WCAR domain as observation. At the upper level (200 hPa), a well-organized Rossby wave train is observed as observation (Fig. 6b). The anticyclonic anomaly dominates East Asia, corresponding to enhanced WCAR. The WAF with respect to the CEP SSTA can be clearly seen in Fig. 7b as originating from the North Pacific, and then traveling across the Atlantic and Europe before ultimately arriving in East Asia, which further confirms that the stationary Rossby wave train stems from the central tropical Pacific.

Figure 8 shows the circulation and rainfall response to the imposed SAT positive SSTA. It can be seen that a robust barotropic Rossby wave train is well reproduced. The SAT SST

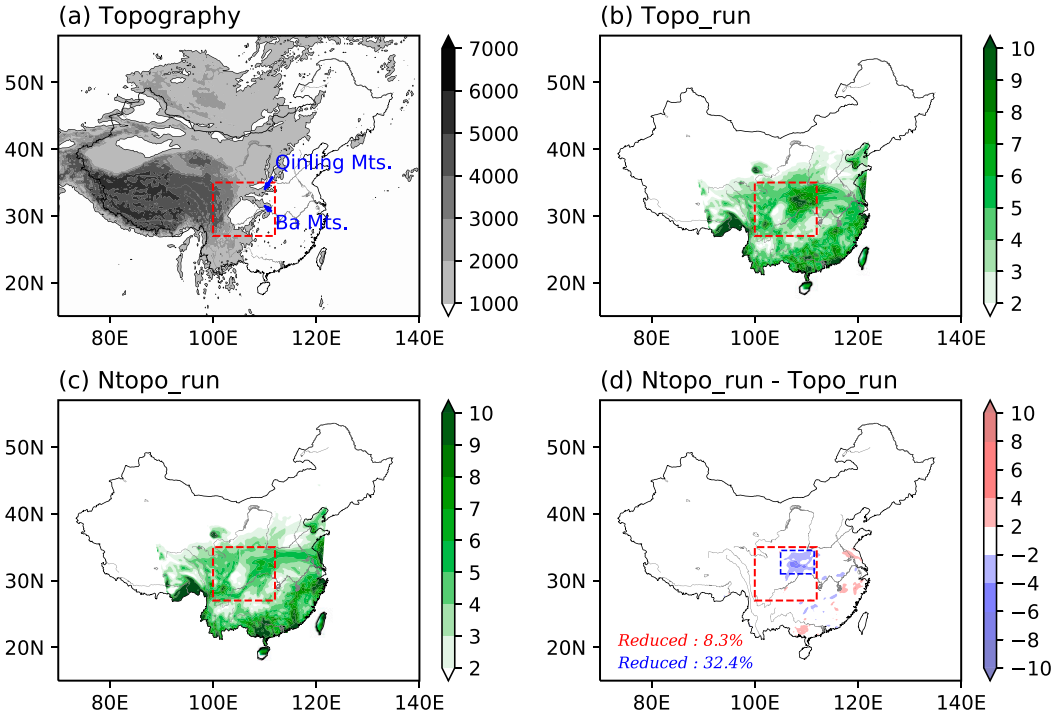

FIG. 9. (a) Topography over the region (gray shading; m). (b) Rainfall rate distribution (shading; mm day^{-1}) in the control experiment. (c) As in (b), but for the sensitivity experiment in which the Qinglin and Ba Mountains were removed. (d) Difference between (b) and (c) (latter minus the former). The red dashed box denotes the WCAR domain, and the blue dashed box denotes the highly mountainous terrain in the WCAR domain.

warming could induce a barotropic high pressure (anticyclonic) anomaly over the subtropical western Atlantic Ocean. The high pressure perturbs the westerly jet stream, leading to the barotropic Rossby wave train over the Eurasian continent. East Asia is dominated by a high pressure (anticyclonic) anomaly at 200 hPa that favors the enhanced WCAR via pumping effect. Note that compared to the location of the upper-level anticyclonic anomaly, the low-level anticyclonic anomaly center shifted slightly southeastward (Figs. 8a,b). The cause of this shift is attributed to the enhanced WCAR itself. Once the rainfall response appears, it could affect low-level circulation through a positive convection–circulation feedback. As a result, the low-level anticyclonic anomaly eventually shifts southeastward relative to the upper-level anticyclonic anomaly. The WAF with respect to the SAT SSTA from the model outputs (Fig. 8b) indicates that the Rossby wave energy propagates from the Atlantic Ocean to northern Europe, and finally arrives in East Asia, causing the anticyclonic anomaly in the region.

To sum up, the CEP negative SSTA and the SAT positive SSTA both could induce the barotropic Rossby wave train, leading to enhanced WCAR. Specifically, the CEP negative SSTA could induce diabatic cooling, which in turn produces the cyclonic anomaly at the upper level in terms of tropical Rossby wave Gill-type response. The cyclonic anomaly perturbs the westerly jet stream. Therefore, it excites the midlatitude Rossby wave train from the North Pacific and propagates downstream of East Asia. Note that this midlatitude Rossby wave train resembles the Pacific–North American–Eurasia (PNE) teleconnection (Chen et al. 2019) observed during the spring and summer season when strong diabatic cooling is observed in the tropical central Pacific during La Niña decaying phase. The Rossby wave train results in the high pressure (anticyclonic) anomaly at the upper level and the horizontal trough at the lower level over central China, leading to enhanced WCAR. The SAT SST warming could excite a local high pressure (anticyclonic) anomaly via longwave radiative heating, which perturbs the westerly jet stream and leads to the Rossby wave train propagating downstream of East Asia, ultimately leading to high pressure at the upper level over East Asia and enhanced WCAR.

4. Effect of real mountains on WCAR

Because WCAR occurs over a mountainous region, it is natural to think that this mountainous topography might have a remarkable impact on the formation of WCAR. Next, we investigate whether this is the case. As shown in Figs. 1d and 9a, the region of maximum WCAR overlaps with two mountain ranges: the Qinglin and Ba Mountains. These two mountain ranges both exceed 1000 m, and the highest peak (Taibai) of the Qinglin Mountains is more than 3700 m. Since the effect of the mountainous terrain on WCAR has not yet been fully understood, in this section we report on the results of two simulation experiments (i.e., the control experiment and the sensitivity experiment) based on the WRF-ARW model to explore this issue.

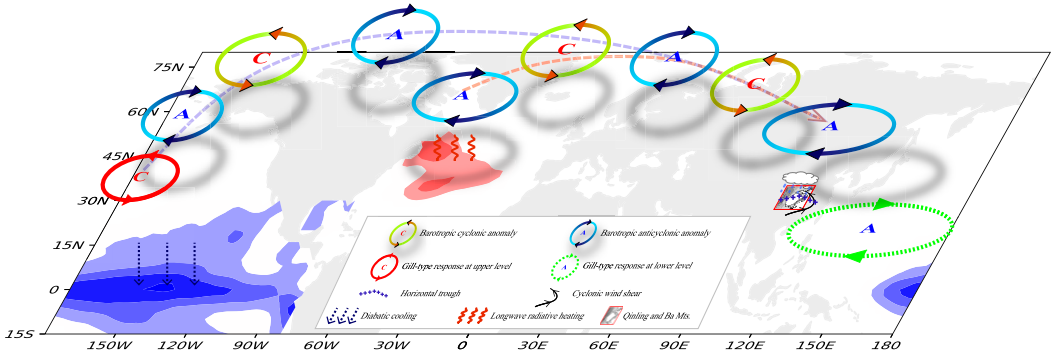

FIG. 10. Schematic diagram illustrating the origin of the interannual variability of WCAR. Gray shading in the red-outlined box denotes the topography, and blue or red shading denotes the CEP negative or SAT positive SST anomaly. Blue and red dashed lines with arrows are the two pathways of the mid- to high-latitude Rossby wave trains induced by SSTA over CEP and SAT.

The control experiment (Topo_run) was integrated from 15 August to 31 October. The integrated outputs from 15 to 31 August were treated as the spinup of the model, and the outputs from 1 September to 31 October were used for diagnosis. The sensitivity experiment was same as the control experiment but run with the removal of the Qinglin and Ba Mountains (Ntopo_run). Figure 9b shows the simulated distribution of the climatological mean (September and October) daily rainfall rate in Topo_run. It is clear that the two maximum rainfall centers of WCAR are nicely reproduced by the WRF-ARW, although the rainfall rate is overestimated over the WCAR domain, as well as over the coastal regions, when compared with the observation as in Fig. 1d. Figure 9c presents the distribution of the daily rainfall rate in Ntopo_run. It suggests that when the mountainous terrain is removed, the rainfall rate over WCAR is slightly reduced, but overall, the rainfall pattern is still robust. The differences between Ntopo_run and Topo_run (Fig. 9d) indicate the effect of the mountains. The rainfall rate is reduced only about 8% over the entire WCAR domain (red dashed box in Fig. 9d), and about 32% over the rainfall maximum domain, which is the very mountainous region (blue dashed box in Fig. 9d). Note, however, that the two maximum rainfall centers of WCAR still appear when the mountains are removed (Fig. 9c), suggesting that the mountainous terrain does not play an essential role in the formation of WCAR. It is understandable that the real mountain ranges do not impact the interannual change of the WCAR, because they could not create the year-to-year variability by themselves. However, the interannual variability of WCAR could be suppressed (with a smaller standard deviation of the interannual variability) without the effect of mountains.

5. Concluding remarks

This paper investigates the origin of the interannual variability of WCAR using observational diagnosis and numerical simulations. The main findings are summarized in Fig. 10. The interannual variability of WCAR is closely related to the horizontal trough or the cyclonic wind shear over the region. The horizontal trough is passively induced by two lower-level anticyclonic (high pressure) anomalies over the East Asian coast. While the anticyclonic anomaly over the south is the Gill-type response to the CEP diabatic cooling, the one over the north is the terminal of two mid- to high-latitude barotropic Rossby wave trains. The formation of these two mid- to high-latitude Rossby wave trains can be traced back to the SSTA over SAT and CEP, respectively. On the one hand, the CEP negative SSTA could suppress the convection and induce diabatic cooling, which stimulates the cyclonic anomaly at the upper level in terms of the Gill-type response, and this cyclonic anomaly perturbs the westerly jet stream, leading to the barotropic Rossby wave train. On the other hand, the SAT positive SSTA could excite a local high pressure (anticyclonic) anomaly via longwave radiative heating, and this perturbs the westerly jet stream, leading to the barotropic Rossby wave train, which overlaps with the one induced by the CEP negative SSTA. The Rossby wave trains result in the configuration of the high pressure (anticyclonic) anomaly at the upper level and the horizontal trough at the lower level over East Asia, leading to enhanced WCAR.

The terminal of the Rossby wave trains, the quasi-barotropic high pressure anomaly over East Asia, acts as an "invisible mountain" that steers the low-level anomalous southwesterly to a southeasterly and hinders the water vapor propagating further to the north. Therefore, enhanced rainfall appears over the cyclonic wind shear region, leading to this special phenomenon of a persistent autumn rainy season, that is, WCAR. On the contrary, the real mountain ranges in the region (the Qinglin and Ba Mountains) have no essential impact on the formation of WCAR. Climatologically, the rainfall rate is reduced only about 8% over the entire WCAR domain, and about 32% over the very mountainous region based on our sensitivity experiment without the terrain of the Qinglin and Ba Mountains.

One may ask whether the circulation anomaly induced by SAT SSTA might be a part of the Rossby wave train induced by CEP SSTA, and the SAT SSTA may partially result from the Rossby wave induced by CEP SSTA and interacts with the Rossby wave. To answer this question, we calculated the correlation coefficient between SAT SST index (areal mean SST over 32°–42°N and 60°–30°W) and CEP SST index (areal mean SST over 5°S–5°N and 175°E–120°W) and only found that neither the original indices nor the detrended indices show any correlation (with correlation coefficients of 0.03 and −0.14,

respectively), suggesting the independence of the SST over CEP and SAT (see Fig. S5 in the online supplemental material). The relationship between these two regions may build up via the atmospheric bridge (e.g., Pacific North America pattern) (Jiang and Li 2019), but this only occurred in winter or spring.

Meanwhile, no significant linkage between the thermal condition over Tibetan Plateau and the WCAR can be found, possibly due to the weakening heating effect of Tibetan Plateau in autumn (see Fig. S6 in the online supplemental material). This further confirms that the horizontal trough is a passive result of the two anticyclonic anomalies on the East Asian coast, rather than a consequence of the Tibetan Plateau thermal forcing.

In the present study, we focus on the interannual connection between CEP/SAT SST and WCAR. In fact, we also found an interdecadal change in the interannual relationship between WCAR and CEP/SAT SST around the mid-1980s. Before the mid-1980s, the WCAR is highly correlated with the CEP SSTA, but after the mid-1980s, it became more related to SAT SSTA. This interdecadal change in the SST forcing region also suggests that the SAT SSTA could independently play a role in driving the interannual variability of WCAR. The reason for this interdecadal change may be attributed to the Atlantic Ocean warming trend, the change of the ENSO property, or the modulation of the interdecadal modes (Pacific decadal oscillation, interdecadal Pacific oscillation, Atlantic multidecadal oscillation, etc.). Currently, we are addressing this issue, and the result will be reported elsewhere.

Acknowledgments. This work was supported by the National Key R&D Program of China (Grant 2018YFC1505905) and the National Natural Science Foundation of China (Grants 41805048 and 41605035). Author Z. W. Zhu is supported by the Young Elite Scientists Sponsorship Program by CAST (Grant 2018QNRC001).

REFERENCES

Bai, H., and W. Dong, 2004: Climate features and formation causes of autumn rain over southwest China (in Chinese). *Plateau Meteor.*, **23**, 884–889.

Chen, M., P. Xie, J. E. Janowiak, and P. A. Arkin, 2002: Global land precipitation: A 50-yr monthly analysis based on gauge observations. *J. Hydrometeor.*, **3**, 249–266, https://doi.org/10.1175/1525-7541(2002)003<0249:GLPAYM>2.0.CO;2.

Chen, S., Z. Zhu, Z. Ge, Z. Kang, and J. He, 2019: The diversity of La Niña decay and the corresponding spring and summer precipitation anomalies over eastern China. *Int. J. Climatol.*, **39**, 3396–3411, https://doi.org/10.1002/joc.6100.

Chen, Z., F. Liu, P. Zhao, and Z. Ma, 2001: Relationship between the surface heating fields over Qinghai-Xizang Plateau and precipitation of southwest China in autumn (in Chinese). *Plateau Meteor.*, **20**, 94–99.

Gao, Y., and Q. Guo, 1958: On the autumn raining area in China (in Chinese). *Acta Meteor. Sin.*, **29**, 264–273.

Gill, A. E., 1980: Some simple solutions for heat-induced tropical circulations. *Quart. J. Roy. Meteor. Soc.*, **106**, 447–462, https://doi.org/10.1002/qj.49710644905.

Gu, W., L. Wang, W. Li, L. Chen, and C. Sun, 2015: Influence of the tropical Pacific east–west thermal contrast on the autumn precipitation in south China. *Int. J. Climatol.*, **35**, 1543–1555, https://doi.org/10.1002/joc.4075.

Hong, S., Y. Noh, and J. Dudhia, 2006: 2006: A new vertical diffusion package with an explicit treatment of entrainment processes. *Mon. Wea. Rev.*, **134**, 2318–2341, https://doi.org/10.1175/MWR3199.1.

Hu, H., Q. Wu, and Z. Wu, 2018: Influences of two types of El Niño event on the northwest Pacific and tropical Indian Ocean SST anomalies. *J. Oceanol. Limnol.*, **36**, 33–47, https://doi.org/10.1007/s00343-018-6296-5.

Huang, B., and Coauthors, 2017: Extended Reconstructed Sea Surface Temperature, version 5 (ERSSTv5): Upgrades, validations, and intercomparisons. *J. Climate*, **30**, 8179–8205, https://doi.org/10.1175/JCLI-D-16-0836.1.

Iacono, M. J., J. S. Delamere, E. J. Mlawer, M. W. Shephard, S. A. Clough, and W. D. Collins, 2008: Radiative forcing by long-lived greenhouse gases: Calculations with the AER radiative transfer models. *J. Geophys. Res.*, **113**, D13103, https://doi.org/10.1029/2008JD009944.

Ji, G., and R. Xu, 1990: Relationship between the surface net radiation in the western Qinghai-Xizang Plateau and the precipitation in China (in Chinese). *Plateau Meteor.*, **9**, 22–31.

Jiang, L., and T. Li, 2019: Relative roles of El Niño-induced extratropical and tropical forcing in generating tropical North Atlantic (TNA) SST anomaly. *Climate Dyn.*, **53**, 3791–3804, https://doi.org/10.1007/s00382-019-04748-7.

Jiang, Z., Z. Ma, and J. Liu, 2014: A study of improved index and climatological characters of autumn rain in western China (in Chinese). *Chin. J. Atmos. Sci.*, **38**, 32–44.

Kain, J. S., 2004: The Kain–Fritsch convective parameterization: An update. *J. Appl. Meteor.*, **43**, 170–181, https://doi.org/10.1175/1520-0450(2004)043<0170:TKCPAU>2.0.CO;2.

Kalnay, E., and Coauthors, 1996: The NCEP/NCAR 40-Year Reanalysis Project. *Bull. Amer. Meteor. Soc.*, **77**, 437–471, https://doi.org/10.1175/1520-0477(1996)077<0437:TNYRP>2.0.CO;2.

Li, D., D. Xu, H. Wang, Q. Qu, and X. Zhao, 2015: Characterization and causal analysis of temporal and spatial variation in dry-wet conditions in autumn in Southwest China. *J. Trop. Meteor.*, **21**, 55–66, https://doi.org/10.16555/j.1006-8775.2015.01.006.

Li, H.-X., H.-P. Chen, and H.-J. Wang, 2017: Influence of North Pacific SST on heavy precipitation events in autumn over North China. *Atmos. Ocean. Sci. Lett.*, **10**, 21–28, https://doi.org/10.1080/16742834.2017.1237256.

Liang, J., 1989: The regional and seasonal distribution of autumn rain in west China (in Chinese). *Sci. Geogr. Sin.*, **9**, 51–59.

Liu, X., and H. Yuan, 2006: Effects of ENSO on the relationship between IOD and autumn rainfall in China (in Chinese). *J. Nanjing Inst. Meteor.*, **29**, 762–768.

Lu, R., Z. Zhu, T. Li, and H. Zhang, 2020: Interannual and interdecadal variabilities of spring rainfall over Northeast China and their associated sea surface temperature anomaly forcings. *J. Climate*, **33**, 1423–1435, https://doi.org/10.1175/JCLI-D-19-0302.1.

Lu, W., 1944: An introduction for China climate (in Chinese). *Meteor. Mag.*, **1**, 2.

Luo, X., D. Li, and H. Wang, 2013: New evolution features of autumn rainfall in West China and its responses to atmospheric circulation (in Chinese). *Plateau Meteor.*, **32**, 1019–1031.

Ma, Z., J. Liu, S. Zhang, W. Chen, and S. Yang, 2013: Observed climate changes in southwest China during 1961–2010. *Adv. Climate Change Res.*, **4**, 30–40, https://doi.org/10.3724/SP.J.1248.2013.00030.

Matsuno, T., 1966: Quasi-geostrophic motion in the equatorial area. *J. Meteor. Soc. Japan*, **44**, 25–43, https://doi.org/10.2151/jmsj1965.44.1_25.

Morrison, H., G. Thompson, and V. Tatarskii, 2009: Impact of cloud microphysics on the development of trailing stratiform precipitation in a simulated squall line: Comparison of one- and two-moment schemes. *Mon. Wea. Rev.*, **137**, 991–1007, https://doi.org/10.1175/2008MWR2556.1.

Niu, N., and J. P. Li, 2008: Interannual variability of autumn precipitation over South China and its relation to atmospheric circulation and SST anomalies. *Adv. Atmos. Sci.*, **25**, 117–125, https://doi.org/10.1007/s00376-008-0117-2.

Roeckner, E., and Coauthors, 1996: The atmospheric general circulation model ECHAM-4: Model description and simulation of present-day climate. Max-Planck-Institute for Meteorology Rep. 218, 90 pp., http://www.mpimet.mpg.de/fileadmin/publikationen/Reports/MPI-Report_218.pdf.

Sun, B., and H. Wang, 2015: Inter-decadal transition of the leading mode of inter-annual variability of summer rainfall in East China and its associated atmospheric water vapor transport. *Climate Dyn.*, **44**, 2703–2722, https://doi.org/10.1007/s00382-014-2251-0.

——, ——, and B. Zhou, 2019: Interdecadal variation of the relationship between East Asian water vapor transport and tropical Pacific sea surface temperatures during January and associated mechanisms. *J. Climate*, **32**, 7575–7594, https://doi.org/10.1175/JCLI-D-19-0290.1.

Sun, L., C. Zhang, H. Zhao, J. Lin, and W. Qu, 2013: Features of climate change in northwest China during 1961–2010. *Adv. Climate Change Res.*, **4**, 12–19, https://doi.org/10.3724/SP.J.1248.2013.00012.

Takaya, K., and H. Nakamura, 2001: A formulation of a phase-independent wave-activity flux for stationary and migratory quasigeostrophic eddies on a zonally varying basic flow. *J. Atmos. Sci.*, **58**, 608–627, https://doi.org/10.1175/1520-0469(2001)058<0608:AFOAPI>2.0.CO;2.

Ting, W., S. He, Q. Yan, W. Dong, and X. Wen, 2018: Decadal shift in west China autumn precipitation and its association with sea surface temperature. *J. Geophys. Res. Atmos.*, **123**, 835–847, https://doi.org/10.1002/2017JD027092.

Wang, B., R. Wu, and X. Fu, 2000: Pacific–East Asian teleconnection: How does ENSO affect East Asian climate?. *J. Climate*, **13**, 1517–1536, https://doi.org/10.1175/1520-0442(2000)013<1517:PEATHD>2.0.CO;2.

Wang, H., Z. Wang, K. Wang, C. Peng, and Y. Zhu, 2018: Circulation characteristics and causes of autumn rain in west China in 2017 (in Chinese). *J. Arid Meteor.*, **36**, 743–750.

Wang, L., W. Chen, W. Zhou, and G. Huang, 2015: Teleconnected influence of tropical northwest Pacific sea surface temperature on interannual variability of autumn precipitation in southwest China. *Climate Dyn.*, **45**, 2527–2539, https://doi.org/10.1007/s00382-015-2490-8.

Wang, Z., and B. Zhou, 2019: Observed decadal transition in trend of autumn rainfall over Central China in the late 1990s. *J. Climate*, **32**, 1395–1409, https://doi.org/10.1175/JCLI-D-18-0112.1.

Wu, B., T. Zhou, and T. Li, 2009: Seasonally evolving dominant interannual variability modes of East Asian climate. *J. Climate*, **22**, 2992–3005, https://doi.org/10.1175/2008JCLI2710.1.

Wu, J., and X. Gao, 2013: A gridded daily observation dataset over China region and comparison with the other datasets. *Chin. J. Geophys.*, **56**, 1102–1111.

Xiao, M., Q. Zhang, and V. P. Singh, 2015: Influences of ENSO, NAO, IOD and PDO on seasonal precipitation regimes in the Yangtze River basin, China. *Int. J. Climatol.*, **35**, 3556–3567, https://doi.org/10.1002/joc.4228.

Xie, S.-P., K. Hu, J. Hafner, H. Tokinaga, Y. Du, G. Huang, and T. Sampe, 2009: Indian Ocean capacitor effect on Indo–western Pacific climate during the summer following El Niño. *J. Climate*, **22**, 730–747, https://doi.org/10.1175/2008JCLI2544.1.

Xu, K., C. Zhu, and W. Wang, 2016: The cooperative impacts of the El Niño–Southern Oscillation and the Indian Ocean dipole on the interannual variability of autumn rainfall in China. *Int. J. Climatol.*, **36**, 1987–1999, https://doi.org/10.1002/joc.4475.

Zhang, C., Z. Wang, B. Zhou, Y. Li, H. Tang, and B. Xiang, 2018: Trends in autumn rain of West China from 1961 to 2014. *Theor. Appl. Climatol.*, **135**, 533–544, https://doi.org/10.1007/s00704-017-2361-9.

Zhao, Z., Q. Li, L. Yi, Z. Zhang, and Z. Zhao, 2000: Relationships between ENSO and climate change in China and predictions of ENSO. *World Resour. Rev.*, **12**, 269–279.

Zhu, Z., J. He, and L. Qi, 2012: Seasonal transition of East Asian subtropical monsoon and its possible mechanism. *J. Trop. Meteor.*, **18**, 305–313.

——, T. Li, and J. He, 2014: Out-of-phase relationship between boreal spring and summer decadal rainfall changes in southern China. *J. Climate*, **27**, 1083–1099, https://doi.org/10.1175/JCLI-D-13-00180.1.

Supplemental Material

Journal of Climate

Supplementary information for

Dynamic origin of the interannual variability of West China autumn rainfall

Zhiwei Zhu[1], Rui Lu[1], Huiping Yan[1], Wenkai Li[1], Tim Li[1,2], Jinhai He[1]

1, Key Laboratory of Meteorological Disaster, Ministry of Education (KLME)/Joint International Research Laboratory of Climate and Environment Change (ILCEC)/Collaborative Innovation Center on Forecast and Evaluation of Meteorological Disasters (CIC-FEMD), Nanjing University of Information Science and Technology, Nanjing, China

2, International Pacific Research Center and Department of Atmospheric Sciences, University of Hawaii at Manoa, Honolulu, Hawaii

Corresponding author: Zhiwei Zhu, Nanjing University of Information Science and Technology, Ningliu Road 219, Meteorology Bldg. Jiangsu 210044, China. E-mail: zwz@nuist.edu.cn

This file includes:

Supplementary figures S1-S6

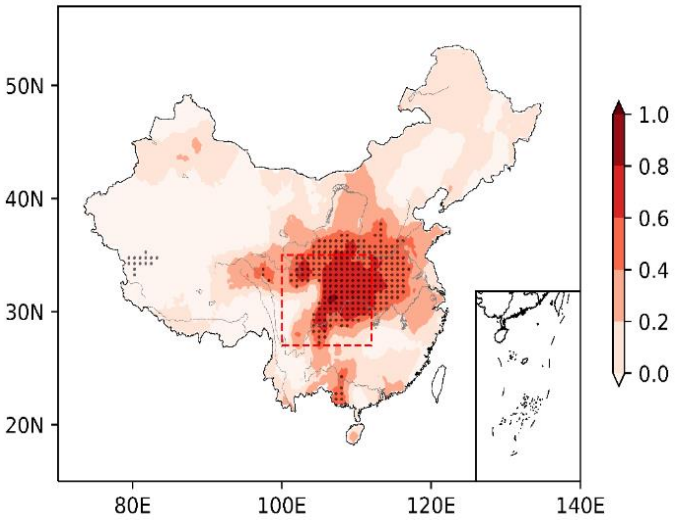

Figure S1. The correlation coefficient map between WCAR index and autumn mean (September and October) precipitation in each grid over China. The black dots mark those correlation coefficients passing the 95% significance level, and the red box denotes the WCAR domain.

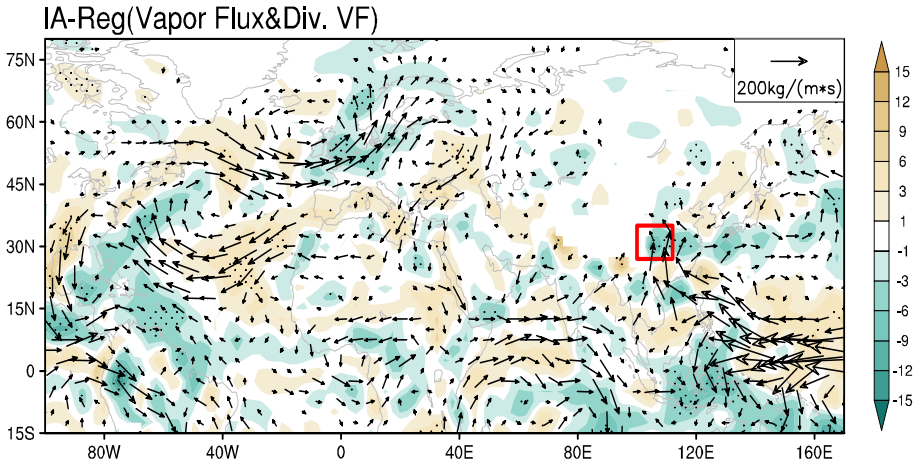

Figure S2. The vertical integrated (from 1000hPa to 700hPa) vapor flux (vectors; 10^{-3}kg m^{-1}s^{-1}, only vectors passing the 95% significant level are shown) and its divergence (shading; 10^{-7}kg m^{-2}s^{-1}hPa^{-1}) regressed onto the interannual variability of WCAR. The black dots mark those regression coefficients passing the 95% significance level, and the red box denotes the WCAR domain.

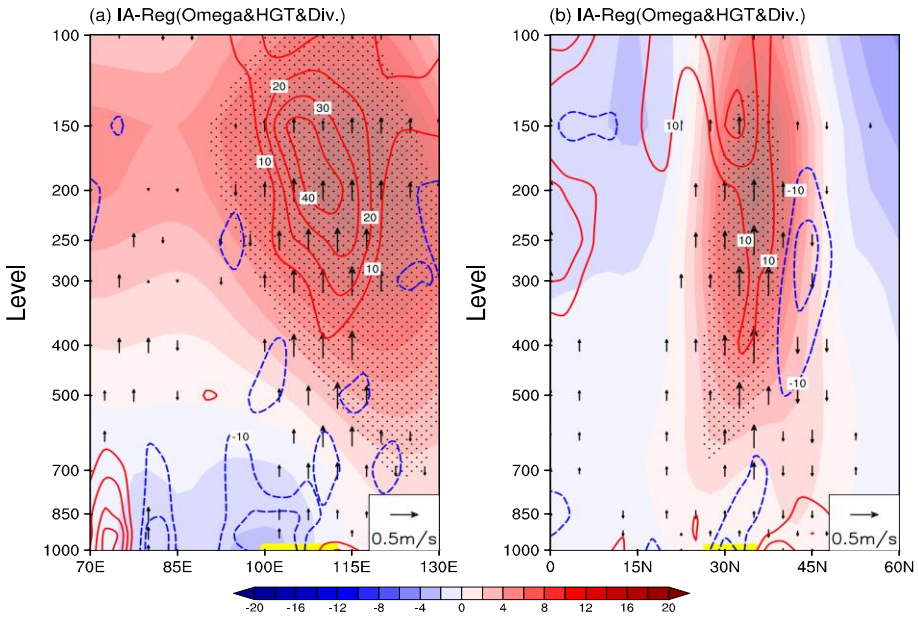

Figure S3. (a) Vertical–longitude profile of geopotential height (shading; gpm), vertical motion (vectors; m s^{-1}, only vectors passing the 95% significant level are shown) and divergence (contours; $10^{-7}s^{-1}$) regressed onto the interannual variability of WCAR averaged over 27°N–40°N. (b) Vertical–latitude profile of geopotential height (shading; gpm), vertical motion (vectors; m s^{-1}, only vectors passing the 95% significant level are shown) and divergence (contours; $10^{-7}s^{-1}$) regressed onto the interannual variability of WCAR averaged over 110°E–135°E. The black dots mark those regression coefficients passing the 95% significance level. The yellow bar denotes the WCAR domain.

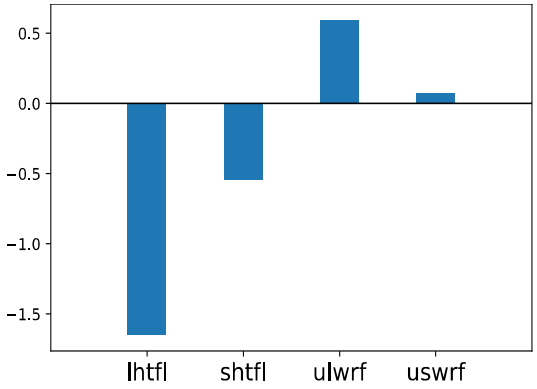

Figure S4. The areal mean regression coefficients of latent heat net flux (lhtfl; W m-2), sensible heat net flux (shtfl; W m-2), upward longwave radiation flux (ulwrf; W m-2) and upward shortwave radiation flux at surface (uswrf; W m-2) over SAT (32°N-42°N, 60°W-30°W) onto the interannual variability of WCAR.

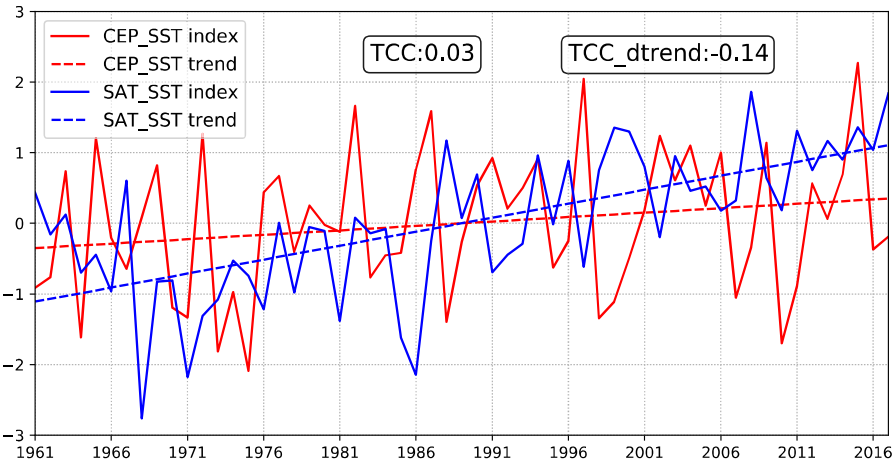

Figure S5. Time series of normalized year-to-year CEP_SST index (areal mean SST over 5°S-5°N and 175°E-120°W, red line) and its trend (red dashed line), SAT_SST index (areal mean SST over 32°N-42°N and 60°W-30°W, blue line) and its trend (blue dashed line).

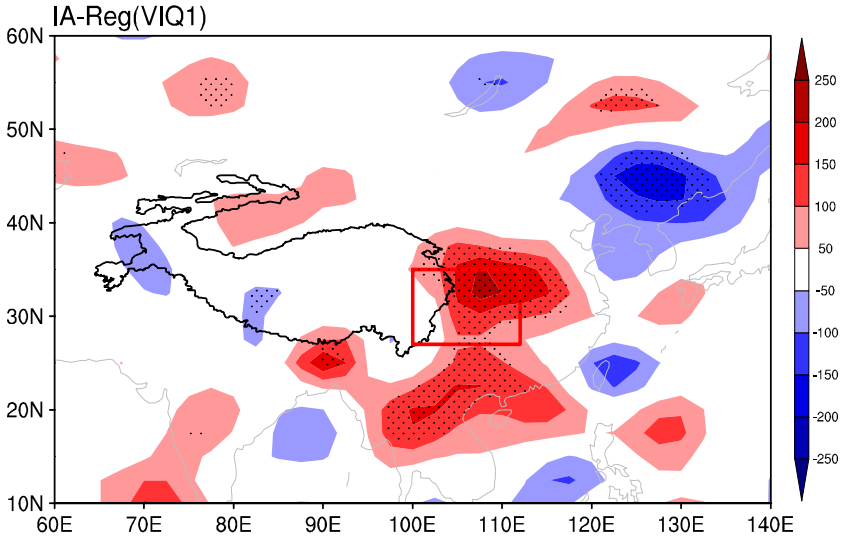

Figure S6. The vertically integrated (from 1000hPa to 300hPa) Q1 (shading; K day^{-1}) regressed onto the interannual variability of WCAR. The black dots mark those regression coefficients passing the 95% significance level, and the red box denotes the WCAR domain. The black solid lines represent the Tibetan Plateau.